



Contents lists available at ScienceDirect

# Engineering Science and Technology, an International Journal

journal homepage: [www.elsevier.com/locate/jestch](http://www.elsevier.com/locate/jestch)

## VeHIF current arcing, volatility and vegetation ignition development: An EMD based volatility analysis for earth-fault classification

Cagil Ozansoy

College Sport, Health and Engineering, Victoria University, Melbourne, Australia



## ARTICLE INFO

**Keywords:**

Empirical mode decomposition  
High impedance fault  
Vegetation  
Volatility

## ABSTRACT

Vegetation High Impedance Fault (VeHIF) events pose severe risks to public safety, wildlife, and forests. Over-current protection schemes generally cannot clear VeHIF events, which have previously resulted in bushfires. This research presents a VeHIF classification method based on the statistical variance analysis of volatility in the empirical mode decomposed feeder current. The author applied the proposed scheme to a dataset of 130 earth-faults with 100 % success rate and a mean classification time of 10 s (standard deviation of 14.32 s). While faster VeHIF fault classification should ideally be achieved, research findings show that faster classification speeds may not always be feasible or necessary. This finding relates to the fact that bushfire risk increases, when charring starts to spread over a branch with a breakout of flames. The present work further validates a positive pairwise correlation between a fault current's volatility and arcing, demonstrating the efficacy of High Frequency (HF) signals as reliable VeHIF volatility signatures.

## 1. Introduction

VeHIFs often result in low fault currents. Traditional overcurrent protection devices generally cannot clear these small fault-current events. If left undetected, VeHIFs pose severe risks to public safety and can ignite fires. The detection of earth faults must ideally occur fast to minimize the bushfire risk. This need, for such a fast response to faults, presents another challenge in ensuring high security to minimize false positives. There is always the need to balance security and speed of a scheme. The HIF current has low magnitude and is volatile with high asymmetry. Generally, electric arcs escort VeHIFs, and HF signatures are released during this process. Literature poorly covers HF signatures, possibly due to the computational burden and the cost of sampling at higher rates. In [1], authors demonstrated that the zero-crossing arcs have varying widths, causing various different levels of HF noise bursts. The study observed HF transients of higher amplitude as the fault current ( $I_f$ ) becomes more aggressively distorted at zero crossings. HIF models are widely used in the literature to apply different techniques (including wavelets, multiresolution, or statistical methods) for detecting HIF events. One concern with existing HIF electrical models is the stationary and steady arcing that such electrical HIF models produce with the same pattern, width, or level from fault inception to end.

This paper contributes to the body of knowledge on the HIF phenomena. Key focus is on the temporal variation and growth of arcing and

volatility during HIFs. This work articulately presents an experimental big-data analysis to address one key weakness of HIF models in representing HIF arcing and volatility. It highlights the various stages of vegetation ignition development, connecting the growth of arcing and volatility (in  $I_f$ ) to the physical process of charring that the vegetation experiences during a VeHIF. This work presents a new method for VeHIF classification based on the Empirical Mode Decomposition (EMD) of the feeder current. Variance analysis of the rate of change in the IMF1 sub-band is at the core of the proposed method. This variance analysis of the IMF1 sub-band's volatility will be referred to as the 'volatility-variance' from here onwards. Key contributions to novel knowledge herein (on the HIF phenomena) can be summarized as follows:

- Arcing is intermittent with fluctuating levels due to conduction through a non-linear impedance. The work identified that fault current arcing grows larger as fault progresses. There is a positive pairwise correlation between the fault current's volatility and arcing. Both volatility and arcing often reach their maximums after carbonization (charring) begins to spread on the surface of the vegetation branch.
- The author studied a few Intrinsic Mode Function (IMF) sub-bands for their volatility-variance correlation with the fault current ( $I_f$ ). IMF1, covering the 1.41 kHz to 44.8 kHz frequency range, had a mean Pairwise Correlation Coefficient (PCC) of 0.99 with a Standard

E-mail address: [cagil.ozansoy@vu.edu.au](mailto:cagil.ozansoy@vu.edu.au).

<https://doi.org/10.1016/j.jestch.2023.101561>

Received 13 July 2023; Received in revised form 17 October 2023; Accepted 22 October 2023

Available online 17 November 2023

2215-0986/© 2023 Karabuk University. Publishing services by Elsevier B.V. This is an open access article under the CC BY license (<http://creativecommons.org/licenses/by/4.0/>).

Deviation (STD) of 0.016 ( $\pm 1.61\%$ ). This high correlation implies that volatility patterns (during VeHIFs) cannot reliably be detected with sampling rates less than 100 kSa/s.

- The IMF1 ‘volatility-variance’ based analysis was applied to a dataset of 130 earth-faults with 100 % success and a mean classification time of 10 s (standard deviation of 14.32 s). The method classified 23 % of the tests in under 2 s and 1.5 % in over 70 s. Network disturbances (e.g. capacitor switching) can also produce volatility, but this volatility is short-lived and quickly dissipates. Conversely, VeHIF volatility signatures are long lasting, unstable, and random. The proposed method was resilience-tested using a VSD-controlled motor switching disturbance. This verification did not produce a false positive, as the set volatility-variance threshold was not violated.

## 2. Literature review

HIF currents are often accompanied by electric arcs for which mathematical models exist [2]. These models have evolved since Cassie [3] and Mayr [4] first described arc conductivity using first-order differential equations. Fig. 1 shows a popular HIF electrical model [2,3] based on two anti-parallel DC sources and diodes. Modifications to this base model exist with variable resistors and inductors added to each arm of the anti-parallel section. Fig. 1 also shows the  $I_f$  generated, using this model, in Simulink. A key concern is that arcing (as modeled by electrical HIF models) is fixed with the same pattern, width, or level from fault inception to end. This paper will demonstrate that HIF arcs grow larger (often there are no arcs for many seconds post fault inception) as fault progresses. A second highlight herein will be validation of the positive correlation between arcing and  $I_f$  volatility.

Asymmetry, non-linearity, intermittency, and randomness are typical HIF features, as reported in [5]. Kavaskar and Mohanty have characterized the HIF current as a low-magnitude, unstable, and fluctuating current [6]. In [7], Ozansoy and Gomes linked fault current volatility to the fire-initiation potential of HIF currents. Authors verified that the increase in current volatility (during a VeHIF) corresponds to when the flame (on the contact vegetation sample) extends along the branch, resulting in widespread charring. One conclusion by Marxsen [8] was that when a species undergoes higher degree of charring, the ignition at height is more likely to result in embers with the size/temperature conditions for fire ignition at ground level. In [9], Ozansoy and Gomes presented insights on the HIF current volatility and its implication on fault detection. The diagnosis of relative volatility was applied to detect HIF signatures and branch charring in the RMS current data stream with respect to the stream itself. This contribution differs from [9] in that it demonstrates effectiveness of using the IMF1 sub-band of  $I_f$ , rather than  $I_{f-rms}$ . Furthermore, it presents a detailed application of the

concept to a large dataset of 130 phase-to-earth (ph-to-e) faults, emphasising attainable response times.

The use of EMD in the power system domain has been well-documented [10–15]. In [16], Biswal et al. used Ensemble EMD in conjunction with Hilbert Huang Transform (HHT) to design a differential protection scheme for a shunt-compensated network. The authors estimated the Discrete Teager Energy (DTE) through HHT of the IMF and used the differential DTE from both ends as detectors. Lala and Karimakar utilised an EMD-based approach (with Artificial Neural Network supervised learning) for classifying high impedance arc faults in [17]. Authors presented inclusive results for a detailed analysis of the arcing phenomena. The detailed discussion on application of EMD to the voltage signal is noteworthy, and analysis of IMFs and their respective PSD plots is informative. In [18], Mishra and Rout applied EMD and Hilbert Transform (HT) for feature extraction of a differential energy based input vector and used it for training a machine-learning fault classifier. Bin and Hongchun [19] employed a similar EMD and HT approach (in a resonant grounded network) and applied it to the zero-sequence current for fault localisation. Wang et al. used the IMF energy moment to extract the failure features of a track circuit [20]. None of these prior works analysed a fault current volatility based scheme, and all reported an analysis based on synthetic simulation-based data except for [17].

## 3. Research aims and methodology

This work presents the electrical and physical characterization of ph-to-e vegetation faults, linking  $I_f$  arcing and volatility to various ignition development stages. The study in [21] is one example of pure research on the physical and electrical phenomena of vegetation contacts with distribution conductors. A key objective herein is to demonstrate how  $I_f$  volatility and arcing are linked to various stages of ignition development. This research also highlights the gradual increase in volatility and arcing as carbonization (charring of the branch) spreads over the branch. The author demonstrates this by analysing  $I_f$  progression in exemplar fault current recordings. This makes it possible to link  $I_f$  progression to various physical ignition stages. These ignition stages include contact development, moisture expulsion and progressive charring that a branch experiences when subject to electrical currents. A computational method for identifying the arcing level in  $I_f$  will then be presented. This computational method relies on estimating the number of samples in each 20 ms window recording where  $I_f$  will be in its  $-0.01 \times |I_{f-max}| < I_f < 0.01 \times |I_{f-max}|$  range. This study then presents the correlation between the arcing level and  $I_f$  volatility. Pearson’s linear correlation coefficient,  $\rho$ , is used to quantify correlation levels. The correlation analysis is applied to a dataset of 123 ph-to-e fault tests, including twelve 0.5 A<sub>rms</sub>, fifty-seven 1 A<sub>rms</sub>, and fifty-four 2 A<sub>rms</sub> limit tests (excluding tests ending with a flashover). The analysis will show that in 90 % of the dataset, maximum arcing and volatility occurs by and after 82.28 % and 83.8 % of the overall fault durations consecutively. The mean  $\rho$  (representing the level of correlation between  $I_f$  volatility and arcing) is 0.77 with an STD of 0.195. Similarity level is higher than 0.90 in 25 % of the tests and smaller than 0.73 in 25 % of the tests.

This work presents an EMD-driven volatility-variance method for classifying VeHIFs. The author uses EMD decomposition to validate HF components as the most credible signatures of  $I_f$  volatility. The author uses Pearson’s linear correlation to compute the linear PCC between variances of  $dI_f/dt$  and each one of the  $d(IMF_i)/dt$ . In particular, the variance of  $d(IMF_1)/dt$  has a mean PCC of 0.99 (STD of 0.016). This high PCC shows a near perfect positive correlation between  $d(IMF_1)/dt$  and  $dI_f/dt$  variances. Using this high positive correlation, author proposes a classification scheme relying on variance analysis of  $d(IMF_1)/dt$ . The variance of the no-fault ( $I_L$ ) current’s volatility is first analysed, identifying likely thresholds to signify a VeHIF event. Classification occurs when the set thresholds are violated. The method is then explicitly verified using two recordings: a 2 A<sub>rms</sub> limit fault of the C. Glaucomphylus

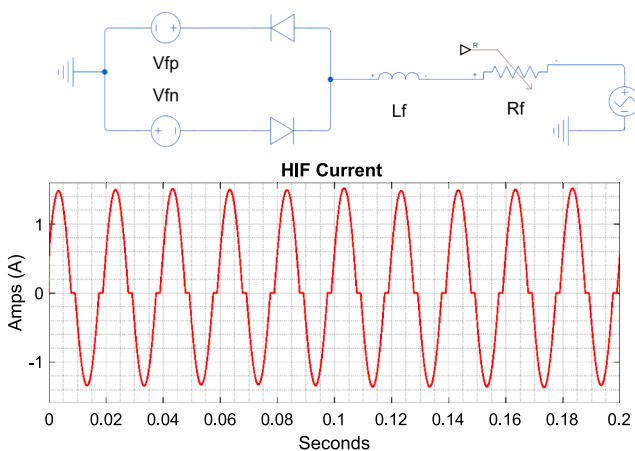


**Fig. 1.** Top: A popular HIF model based on two anti-parallel DC-source and diodes. Bottom: The HIF  $I_f$  generated by the model.

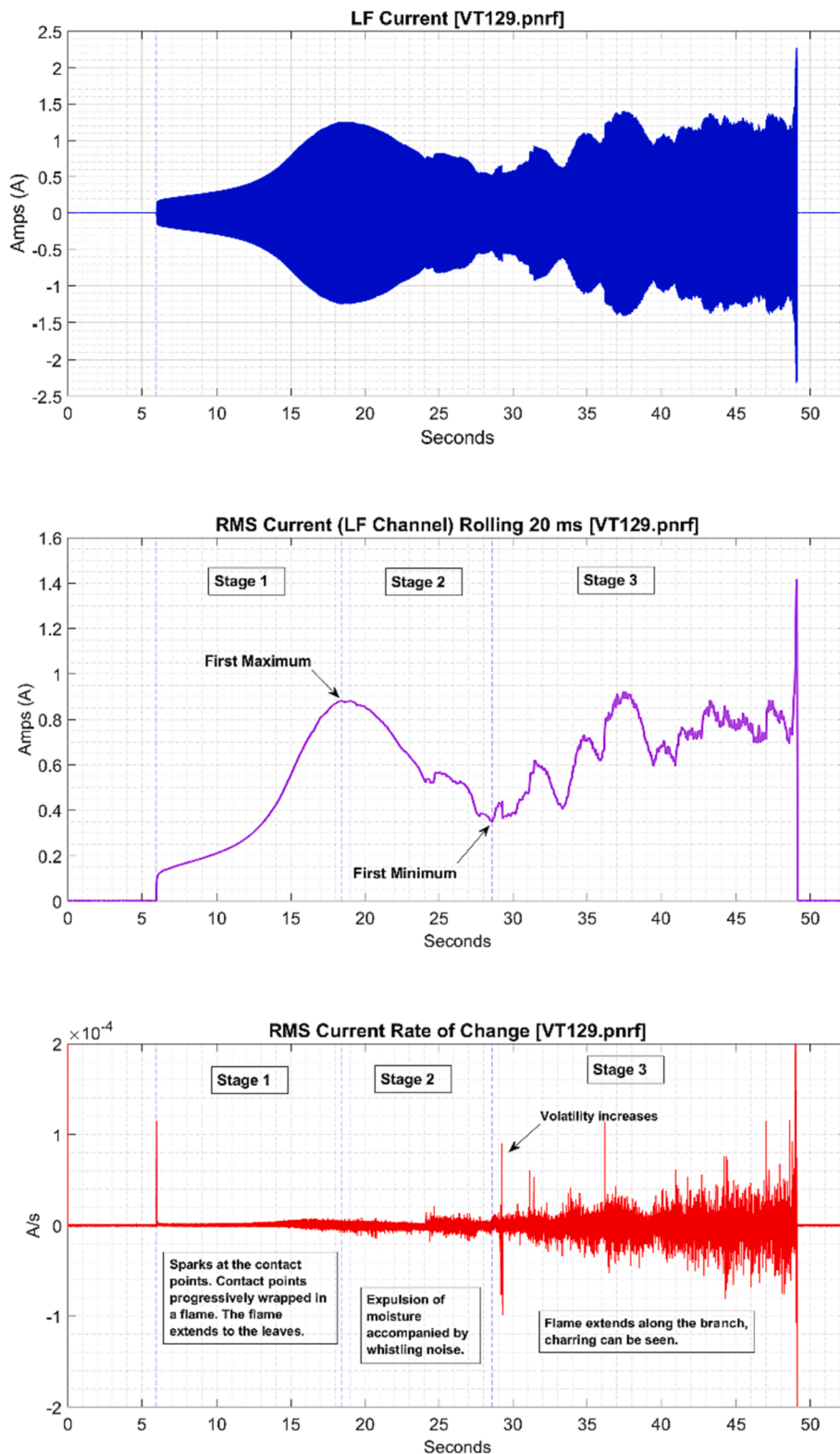


**Fig. 2.** First row: the sampled  $I_f$ . Second row:  $I_{f-rms}$ . Third row:  $dI_{f-rms}/dt$ . (VT129; A. Mearnsii; 1 A<sub>rms</sub> limit).

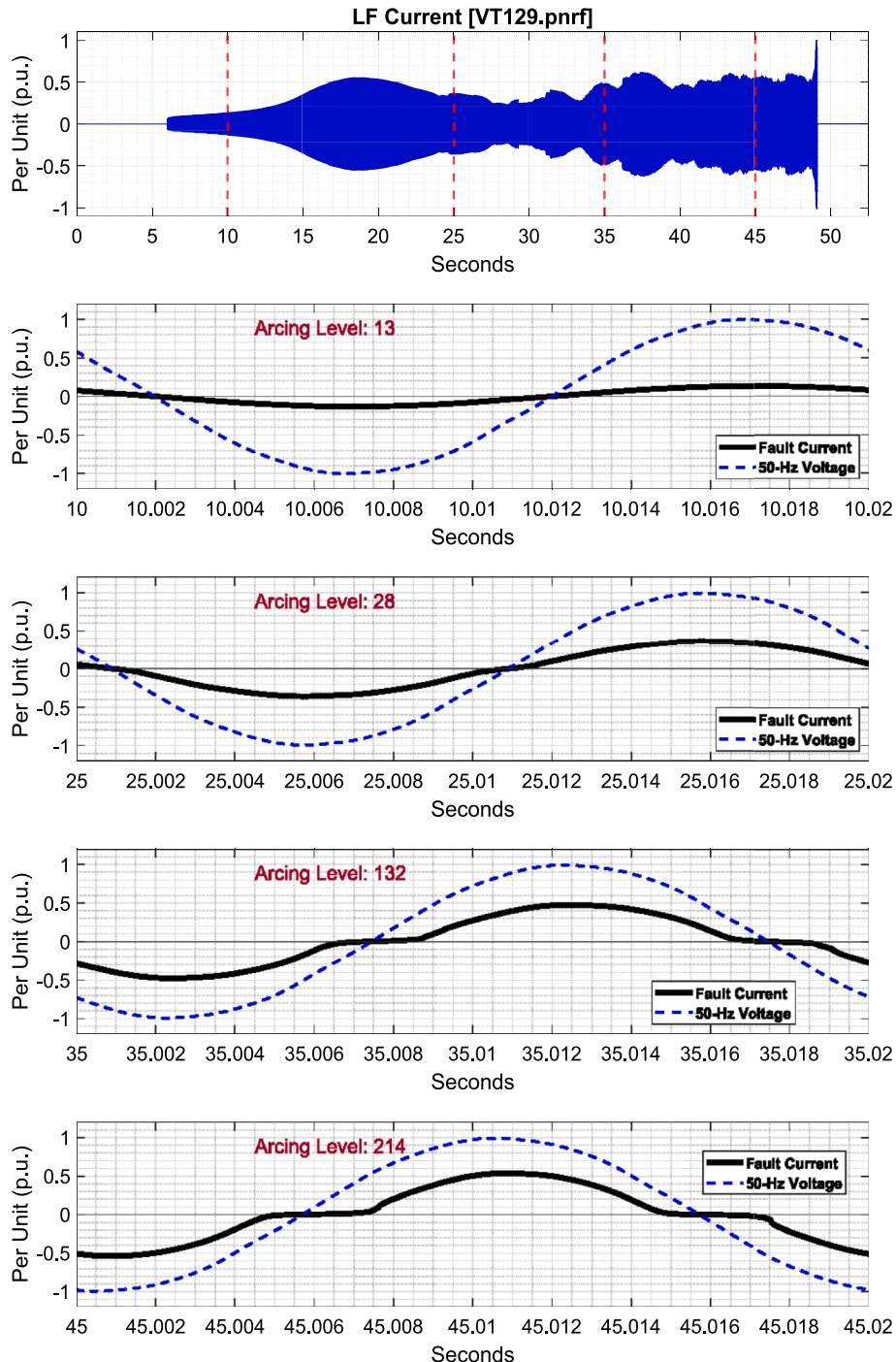


**Fig. 3.** First row: the fault current ( $I_f$ ). Second row: Very low-level of arcing at 10 s. Third row: Low-level of arcing at 25 s. Fourth row: High-level of arcing at 35 s. Fifth row: Very high level of arcing at 45 s. (VT129).

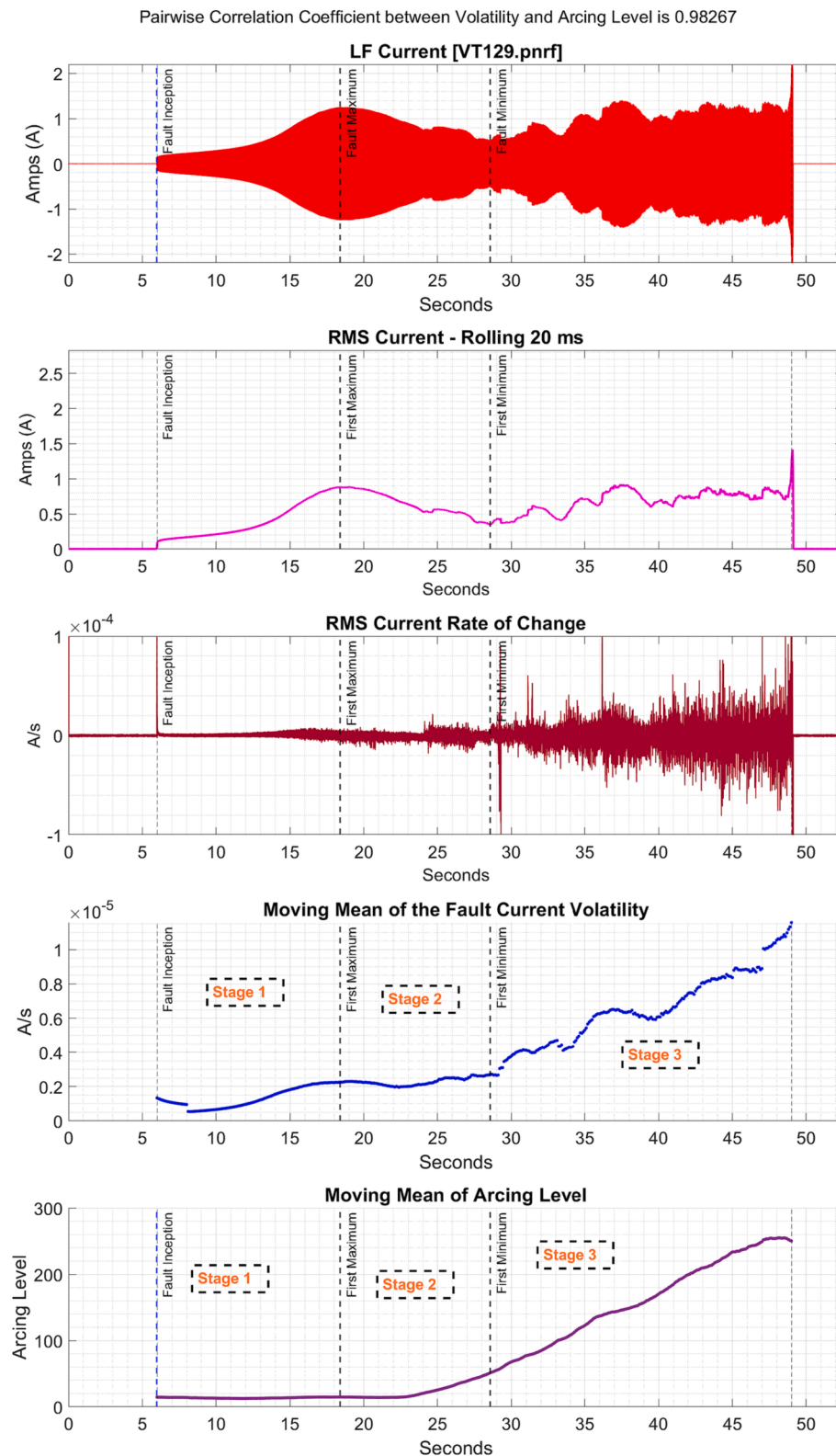


**Fig. 4.** Temporal arcing and volatility variation of  $I_f$ . First row: the sampled fault current. Second row:  $I_{f-\text{rms}}$ . Third row:  $dI_{f-\text{rms}}/dt$ . Fourth row: moving mean of volatility. Fifth row: Moving mean of arcing level. (VT129).

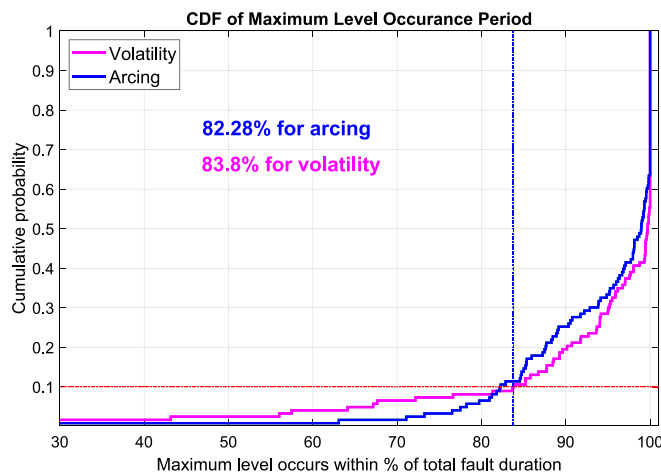


**Fig. 5.** CDF of maximum arcing and volatility level occurrence times as percentage of the overall fault durations of 123 fault tests.

species and a  $0.5 \text{ A}_{\text{rms}}$  limit fault of Eu. Baxteri species. Results show how the volatility-variance of the  $I_f + I_L$  case starts to deviate from the no-fault levels post fault inception. This deviation is due to the fault induced HF components in IMF1. Statistical reliability of the scheme is then validated by testing its application to 130 fault recordings. Finally, the author applies the method to a VSD-controlled motor disturbance, demonstrating the resilience of the scheme against false positives.

#### 4. Stages of ignition development and arcing

The validation dataset employs fault data from staged VeHIFs performed for the ‘Vegetation Conduction Ignition Testing’ project [8]. In the project, ph-to-earth (ph-to-e) fault tests included a tree branch laid across two conductors, one energized with the 12.7 kV phase voltage and the other earthed. The LF channel (DC to 50 kHz) sampled  $I_f$

continuously with a 100 kSa/s sampling rate. Fig. 2 shows the LF recording during a ph-to-e VeHIF test (of A. Mearnsii species) labelled ‘VT129’. The test was terminated after  $I_f$  reached  $1 \text{ A}_{\text{rms}}$ . Various stages of ignition development [8] can be identified for VeHIFs. These are the contact development (Stage 1), moisture expulsion (Stage 2), and progressive charring (Stage 3) [8]. As shown in Fig. 2, Stage 1 is dominated by a progressive increase in the plasma until  $I_f$  reaches its first maximum. In Stage 2,  $I_f$  falls due to the expulsion of the moisture, which dries out the species, resulting in its resistance to increase. Finally, in Stage 3, charring begins accompanied by breakout of flames. During charring, arcs often appear in the flame causing  $I_f$  volatility.  $I_f$  volatility (a sign of charring) begins to peak around the first local minimum (after the first maximum) [7].

Fig. 3 shows the arcing level computation in  $I_f$  at various 20 ms window intervals (time spaced) during the progression of VT129. All waveforms are in p. u. using the base values of  $2.27 \text{ A}$  and  $17.3 \text{ kV}$ . As illustrated in Fig. 3, arcing is intermittent with fluctuating levels due to conduction through a non-linear impedance. When arcing occurs, it extinguishes near the zero-crossings due to inadequate voltage levels for sustaining the discharge. It reignites once voltage recovers to a level where the discharge can be sustained again. These discontinuities near zero-crossings have varying widths and grow larger as fault progresses. The arcing level is computed by estimating the number of samples in each 20-ms window recording, where  $-0.01 \times |I_{f,\text{max}}| < I_f < 0.01 \times |I_{f,\text{max}}|$ . This is based on the premise that a higher number of samples is recorded near zero crossings at times of high arcing.

#### 5. The link between arcing and volatility

Fig. 4 shows the temporal variation of the moving means of  $I_f$ ’s volatility and arcing level. The volatility measure is the 40-sample moving mean of the average  $dI_{f,\text{rms}}/dt$  of 20 ms data blocks taken every 100 ms. The arcing measure is the 40 sample moving mean of the arcing level. The Pearson’s linear correlation coefficient,  $\rho$ , is defined in (1) where  $X_a$  is the volatility measure, and  $Y_b$  is the arcing level

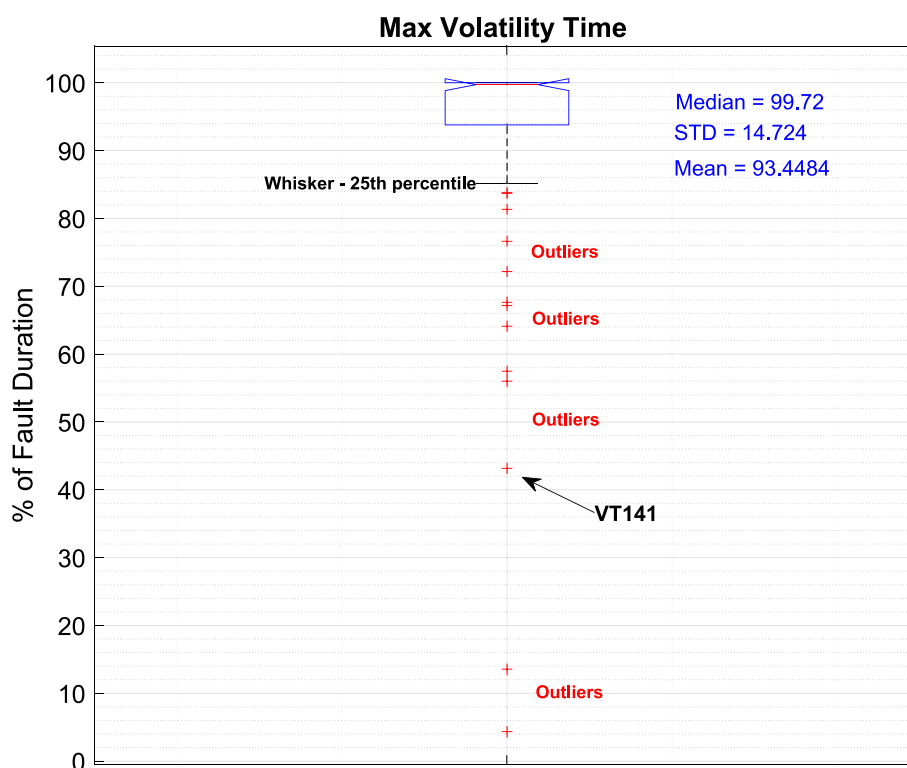


**Fig. 6.** Statistical distribution of the occurrences of maximum volatility times during the progression of faults measured as  $t_{\text{max-volatility}}/t_{\text{fault-duration}}$  percentage.

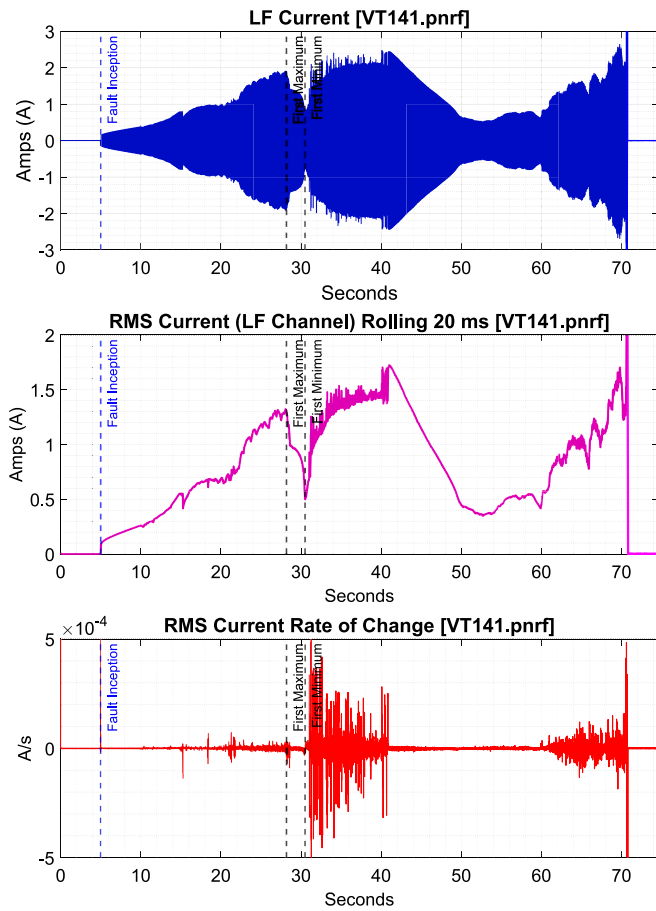


Fig. 7. Top: the sampled  $I_f$ . Centre:  $I_{f\text{-rms}}$ . Bottom:  $dI_{f\text{-rms}}/dt$ . (VT141).

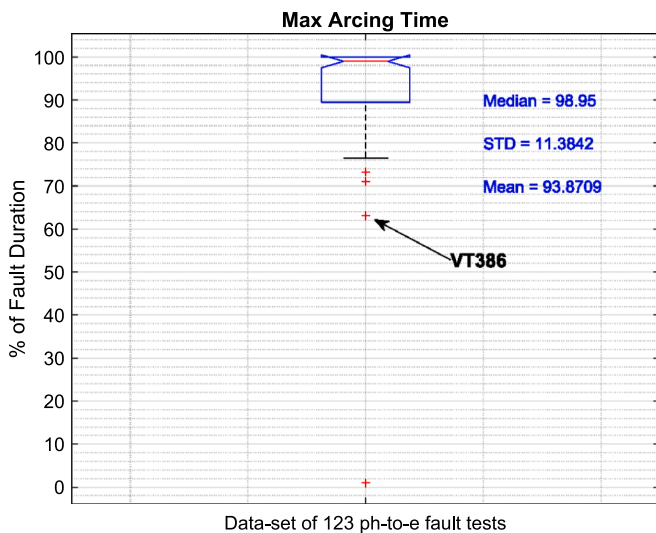


Fig. 8. Statistical distribution of the occurrences of maximum arcing times during the progression of faults measured as  $t_{\text{max-arcing}}/t_{\text{fault-duration}}$  percentage.

measure. The  $\rho$  is used for estimating the level of temporal similarity between the two measures. The  $\rho$  between the two measures was computed as 0.98 for VT129, a near perfect positive correlation (+1 indicates a perfect positive correlation).

$$\rho(a, b) = \frac{\sum_{i=1}^n (X_{a,i} - \bar{X}_a) \times (Y_{b,i} - \bar{Y}_b)}{\sqrt{\sum_{i=1}^n (X_{a,i} - \bar{X}_a)^2} \times \sqrt{\sum_{j=1}^n (Y_{b,j} - \bar{Y}_b)^2}} \quad (1)$$

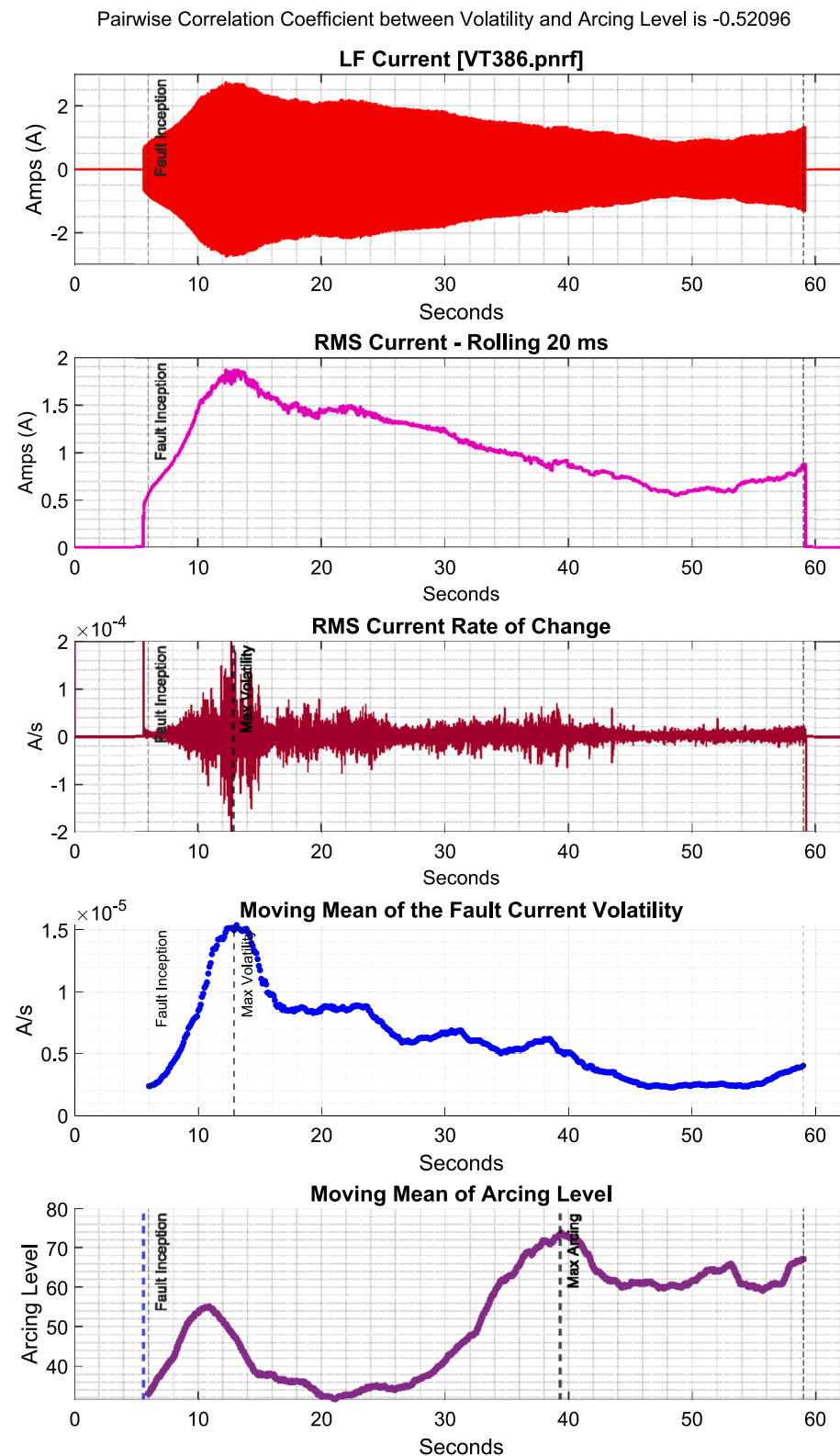
The presented single recording analysis (for VT129) supports the hypothesis that arcing reaches its maximum in Stage 3 when volatility increases. This growth relates to the increased levels of HF noise emissions during Stage 3. As in Fig. 4, arcing is low and steady during Stage 1 when progressive increase in the plasma results in the first  $I_f$  maximum. Volatility is also increasing during Stage 1 as the  $I_f$  magnitude increases. In Stage 2,  $I_f$  falls due to the increasing fault impedance (attributable to expulsion of moisture), but volatility appears to be steady. Arcing increases after the 23 s. This increase continues almost linearly into Stage 3. In Stage 3, both volatility and arcing increase as  $I_f$  peaks with carbonization (charring) breakout. Finally, in Stage 3, charring begins accompanied by flame breakout. During charring, arcs appear in the flame, causing  $I_f$  volatility.  $I_f$  volatility (a sign of charring) peaks around the first local minimum, which comes after the first maximum. The current HIF electrical models can neither accurately model temporal variation of arcing nor  $I_f$  volatility. This weakness is a shortcoming considering the use of such models in academic publications for generating synthetic fault data. The following section seeks to provide further evidence on this claim.

## 6. Big data analysis

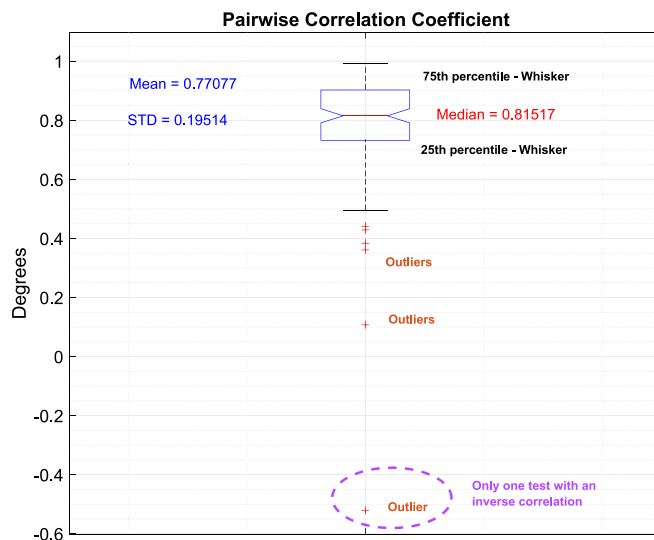
This section analyses the volatility and arcing trends in a dataset of 123 ph-to-e fault tests (twelve 0.5 A, fifty-seven 1 A, and fifty-four 2 A limit tests). Tests, ending with a flashover, were excluded from the analysis based on the recommendation in [4]. The hypothesis of this research is that  $I_f$  arcing and volatility are closely correlated, both often reaching their maxima in Stage 3. The key intent of this section is to generalize this hypothesis statistically. This analysis is additional to the earlier evidence presented using the single fault recording of VT129.

Fig. 5 shows the Cumulative Distribution Function (CDF) of the maximum-level timestamps for arcing and volatility measures as percentages relative to the overall fault durations. It displays the timestamps at which volatility and arcing reached their maximums during the temporal progression of faults within the dataset. In 90 % of the dataset, the maximum arcing level occurred by and after 82.28 % of the overall fault durations. For example, in VT605 (the test at the 90 % boundary), the maximum arcing occurred 58.5 s into the fault. VT605 was terminated at the 71.1 s, when  $I_{f\text{-rms}}$  reached the set current limit. In 90 % of the tests, maximum volatility similarly occurred by and after 83.8 % of the overall fault durations. For example, in VT467 (the test at the 90 % boundary), the maximum volatility level was reached 26.9 s into the fault for an overall fault duration of 32.1 s. These findings support the hypothesis that both arcing and volatility usually grow to their maxima during Stage 3, when carbonization is underway.

Fig. 6 shows the statistical analysis of maximum volatility times ( $t_{\text{max-volatility}}$ ) as percentages of respective fault durations. As shown, the mean  $t_{\text{max-volatility}}$  occurs at approximately 93.45 % of the fault duration with a standard deviation of 14.72 %. The median (red line in the middle of the box plots) is close to 100 %, signifying that volatility generally increases as fault progresses. The bottom and top of the box plot represent the 25th and 75th percentiles, respectively. The distance in between the percentiles is equal to the interquartile range. The whisker extends below the box to the furthest observation within the whisker length. Observations beyond the whisker length are the outliers, which extend more than 1.5 times the interquartile range away from the bottom or top of the box. There were a number of outliers, such as the VT141 (2 A<sub>rms</sub> limit, C. Glaucomorphus species). However, in 90 % of the tested faults, max volatility occurred by and after 83.8 % of the fault duration. Fig. 7 shows the VT141 fault current recording, its  $I_{f\text{-rms}}$ , and  $dI_{f\text{-rms}}/dt$ . VT141 goes through all three stages of ignition development,



**Fig. 9.** First row:  $I_f$ . Second row:  $I_{f-\text{rms}}$ . Third row:  $dI_{\text{rms}}/dt$ . Fourth row: moving mean of volatility. Fifth row: Moving mean of arcing level. (VT386, 2 A limit, Eu. Baxteri)).



**Fig. 10.** Distribution of correlation coefficient between arcing and volatility.

with  $\sim 2$  s separating Stages 1 and 2. In Stage 3,  $I_f$  is very volatile midway through the fault, but unexpectedly decays until it recovers and ramps up around the 60 s mark.

Fig. 8 shows the statistical analysis of the max arcing times ( $t_{\max\text{-arcing}}$ ) as percentages ( $t_{\max\text{-arcing}}/t_{\text{fault-duration}}$ ) of fault durations. For example, in VT767, maximum arcing occurred 66.4 s into the fault, which had a duration of 78.1 s. Maximum arcing occurred at 85 % point of the overall fault duration of VT767. The mean  $t_{\max\text{-arcing}}$  is 93.87 % with an STD of 11.38 %. Fig. 9 shows the VT386  $I_f$  recording, its  $I_{\text{rms}}$ , and moving means of the fault's volatility and arcing. VT386 is an outlier test where max volatility occurred soon after fault inception. For VT386, while arcing was still high at the end of the fault, max arcing occurred at 40 s into the recording.

Another critical observation in VT386 is the inverse correlation between  $I_f$ 's volatility and arcing. As shown in Fig. 9, volatility falls as the fault progresses, while arcing level is increasing. In the entire dataset of 123 ph-to-e fault tests, VT386 was the only test with an inverse correlation between  $I_f$ 's volatility and arcing. As shown in Fig. 8, there were few other outliers (in 90 % of the faults, max arcing occurred by/after 82.28 % of fault durations) as well. The number of outliers (four in total) is smaller when compared to the outliers of the volatility distribution (twelve in total). The increase of arcing as the fault progresses is consequently more consistent in a higher number of tests when compared to volatility.

The box plot of Fig. 10 depicts the statistical analysis of the pairwise linear correlation between volatility and arcing. The mean  $\rho$  was 0.77 with an STD of 0.195. The 25th to 75th percentile range was 0.73 to 0.90. In 25 % of the tests,  $\rho$  was higher than 0.90. Conversely, in only 25 % of the tests,  $\rho$  was smaller than 0.73. There were five outliers extending beyond the lower whisker. These outliers still exhibited a positive pairwise correlation, with the exception of VT386. As shown in Fig. 10, VT386 was the only outlier where  $\rho$  was negative (-0.52), designating an inverse correlation. These results statistically confirm that volatility and arcing are indeed substantially positively correlated.

## 7. VeHIF volatility-variance analysis using EMD

This section analyzes the volatility of VeHIFs currents using EMD. Identifying frequencies that lead to  $I_f$  volatility during a fault is the key objective. EMD is a data-driven and adaptive method of time-domain signal decomposition, which uses the signal as its bases. This is in contrast to wavelet methods, which require the choice of a pre-determined basis or mother wavelet for the decomposition. Fig. 11

shows the EMD of a VeHIF  $I_f$  signal (VT963; 2 A limit; C. Glaucomphylus species), where  $I_f$  has been broken down into a set of IMFs. In Fig. 11, the sampled fault current and its rolling RMS are shown on top of the EMD generated IMFs. IMFs show the sub-signal oscillation modes of dominant frequencies embedded in the  $I_f$  time-sequence. They neatly characterize a finite set of sub-band signals at dominant frequencies over the same time segment.

Welch's method was used to obtain the predominant frequency with the highest spectral density in each IMF. As expected, the highest frequency component was captured by the first IMF. IMF1 covers the 1.41 to 44.8 kHz frequency range with a dominant frequency of 17.84 kHz. The predominant frequency reduces to 0.14 Hz with the increasing IMF order. Both IMF4 and IMF5 have 50 Hz as their predominant frequency mode, indicative of mode-mixing [22] (a common problem in EMD). This finding is similar to the observation made in [17] for the EMD analysis of the arcing voltage. This suggests that the 50 Hz fundamental cannot always contribute to extrema [22] due to the non-linear growth of the fault current. This forces EMD to split the 50 Hz mode over two IMFs. It is also notable to observe the distinct magnitude spike in the HF modes (IMF1 to IMF3) and the Low Frequency (LF) modes (IMF7 to IMF8) a few seconds prior to the conclusion of the test, when  $I_f$  reached the set threshold.

The proposed volatility-variance based classification is based on the cumulative analysis of the variance of  $di/dt$  in each IMF. The variance-based concept explores fluctuations in the volatility of the stream. The stream includes the sliding window of ten most recent samples of the discrete gradient in each IMF. This aids in computationally observing fluctuations in the gradient of each sub-signal, indicative of volatility in that stream. The forward volatility is computed from (1) by calculating rolling average of the variance of a data stream's volatility. The VRate parameter defines the number of samples stored in a computation window. The default VRate is 10, but can be adjusted. The volatility index for each stream (IMF1 to IMF10) is the moving mean of the rolling variance of the stream's rate of change. This is calculated at a rate of 5000 samples, as in (2). This rolling average of the variance of the fault current's volatility ( $di/dt$ ) is termed the 'volatility-variance' index.

$$\sigma_{IMF-z}^2(n) = \text{Var} \left( \frac{dI_{IMF-z}}{dt}(i+1 - VRate) : \frac{dI_{IMF-z}}{dt}(i) \right)$$

for  $i = VRate : VRate : (\text{length}(Current) - VRate)$

$$vol_{indIMF-z}(j) = \frac{1}{N} \times \sum_{k=j}^{j+1+N} \sigma_{IMF-z}^2(k)$$

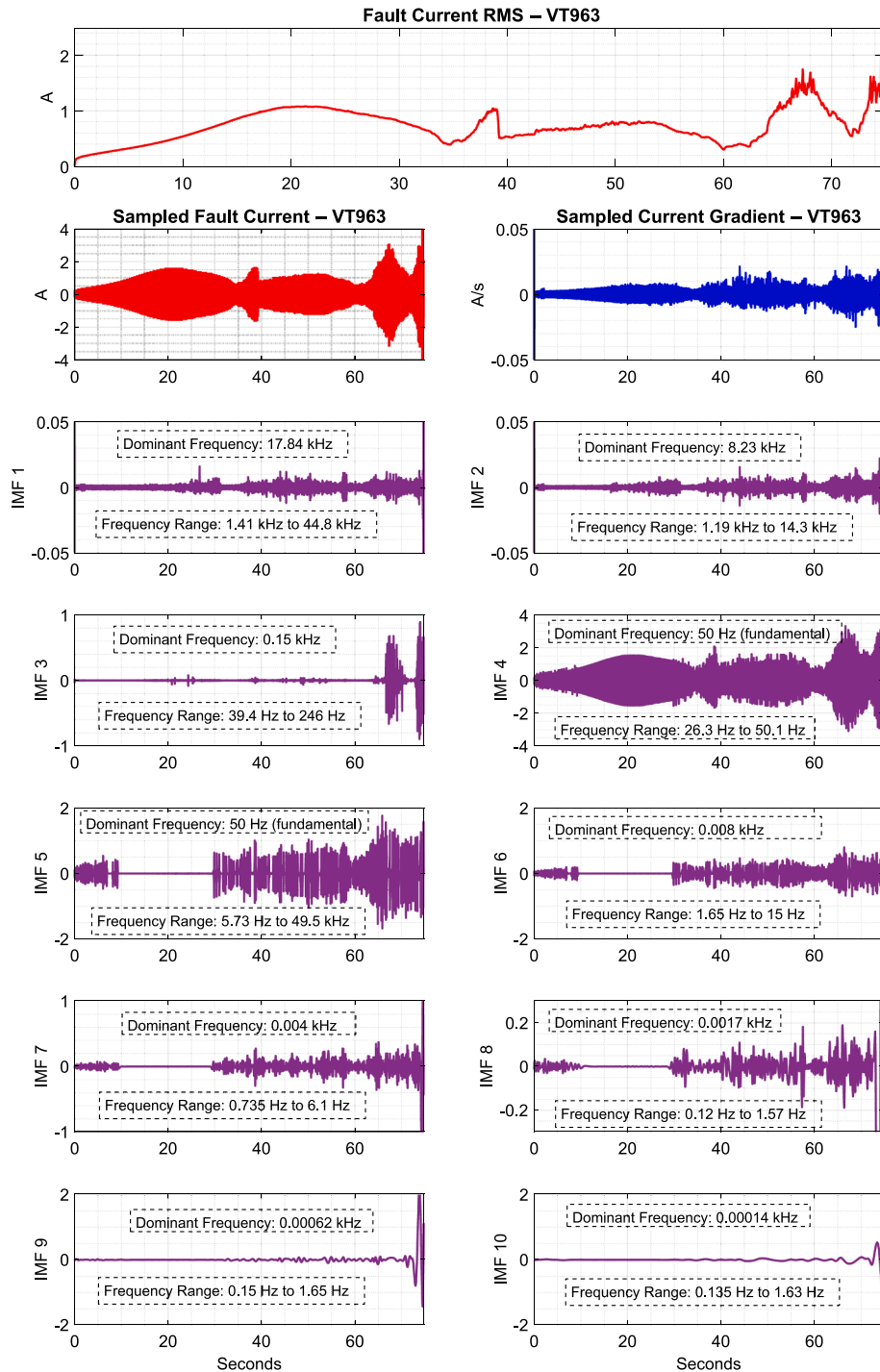
for  $j \geq 1$  and  $N = 5000$

where  $VRate = 10$  samples,

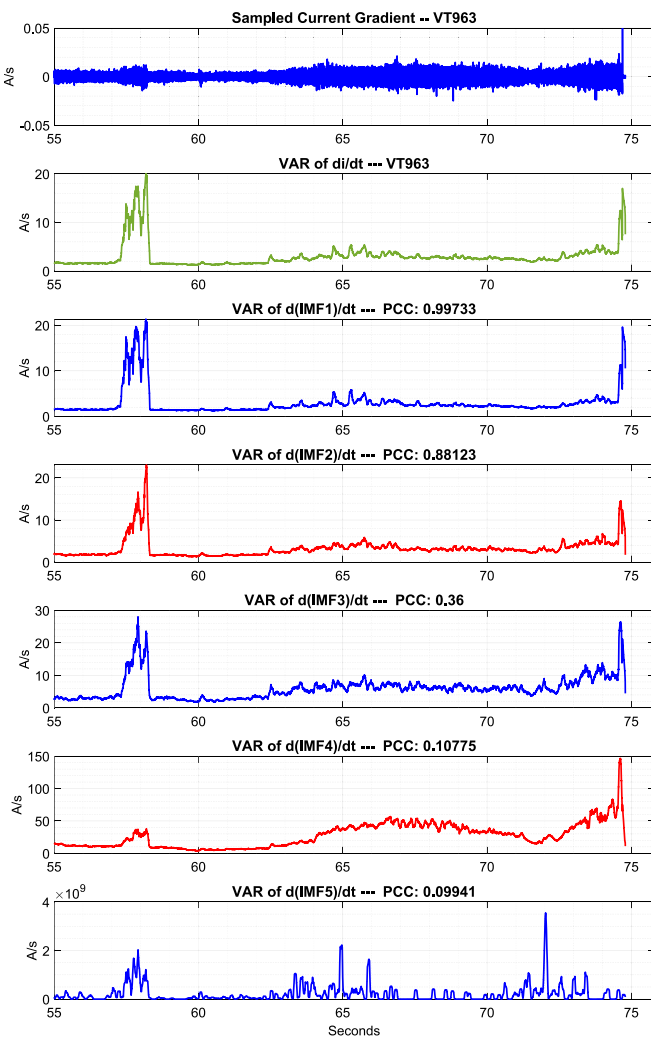
$z$  is the IMF index number,  $n$  is the variance index number,  
 $\sigma_{IMF-z}^2$  is the rolling variance of the  $z^{\text{th}}$  indexed IMF's gradient,  
 $vol_{indIMF-z}$  is the volatility-variance of a  $z^{\text{th}}$  indexed IMF.

Fig. 12 shows the volatility-variance analysis of the sampled  $I_f$  and its first four IMFs from 56 s onwards (in test VT963). Fig. 12 only shows the 56 s onwards segment to enable better visual contrast of the volatility-variance indexes of the data streams. In calculating  $I_f$ 's volatility, volatility indexes were normalized to better capture the volatility trends instead of a magnitude based focus. The Pearson's linear correlation coefficient was used to calculate the Pairwise Correlation Coefficient (PCC) between the variance of  $di_f/dt$  and variances of each  $d(IMF_x)/dt$ . In this case, PCC measures the correlation between  $I_f$ 's volatility and those of the IMF streams. For each IMF mode, its PCC with  $I_f$  has been labelled on top of the respective subplot.

As shown in Fig. 12, IMF1 has a nearly perfect positive correlation (+1 signifies an ideal pairwise correlation) with  $I_f$ . IMF2 also has a good positive correlation. It covers the 1.19 kHz to 14.3 kHz mode range, with



**Fig. 11.** Empirical Mode Decomposition of a VeHIF (VT963; 2 A limit).



**Fig. 12.** Volatility-variance analysis of  $I_f$  and its IMFs (VT963; 56 s onwards). Row one:  $dI_f/dt$ . Rows two to seven: volatility-variance of each data stream.

a dominant frequency of 8.23 kHz. IMF3, which is the volatility of the third harmonic, has a poorer PCC score. From IMF4 onwards, the PCC measures decrease. Both IMF4 and IMF5 (with the dominant frequency of 50 Hz, the fundamental) have low PCCs of around 0.1. This signifies that the volatility of the fault current is mainly due to HF components rather than the 50 Hz fundamental. Therefore, IMF1 dominates the volatility-variance of the current.

The volatility-variance of  $dI_f/dt$  produces an identical trend as the IMF1 (PCC of 0.997), albeit some small magnitude differences. This was anticipated, as it shows that HF terms dominate. This makes the sampling rate a critical factor in the design of protection schemes against VeHIFs. Therefore, a high sampling rate, such as 100 kSa/s, is indeed required for detecting the volatility induced during VeHIFs. In contrast, the 'F60 Feeder Protection System' (marketed for HIF detection capability) has a sampling rate of 3.2 kSa/s (50-Hz frequency system) [23]. Another manufacturer recommends [24] a sample rate of 32 samples per

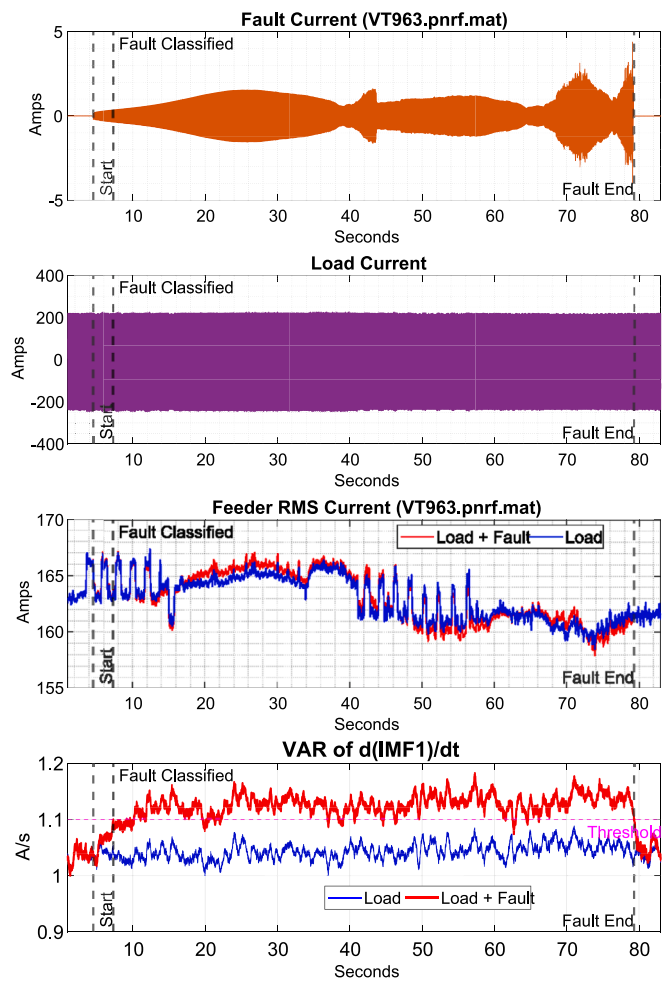


**Fig. 13.** Classification of VT963. First Row: Sampled  $I_f$ . Second Row: Sampled  $I_L$ . Third Row: Rolling RMS currents of  $I_L$  and  $(I_L + I_f)$ . Fourth Row: Volatility of the (i)  $I_L$  only case (blue trace) case (ii)  $I_L + I_f$  (red trace) case. (For interpretation of the references to colour in this figure legend, the reader is referred to the web version of this article.)

cycle, which equates to 1.6 kSa/s (50 Hz system). The proposed sampling rate of 100 kSa/s is even higher than sampling rates of most substation grade power-quality meters (128, 256, or 512 Sa/cycle). Even if the fault current ( $I_f$ ) is sampled at 25 kSa/s (~512 Sa/cycle) or less, some HF signatures will be lost, missing critical volatility patterns. Therefore, VeHIF HF signatures cannot be reliably detected with lower sampling rates.

**Table 1** shows the PCC comparison of IMFs in a large dataset of VeHIF faults. The aim is to verify the statistical significance of HF components over the LF components. For this reason, the rolling variance average of each  $d(IMF_x)/dt$  was determined to compute its linear PCC to the rolling variance average of the  $dI_f/dt$  itself. As in **Table 1**, IMF1 leads with a nearly perfect mean PCC and a very low STD. This result confirms IMF1 as a reliable sub-band for volatility detection during VeHIF events.

**Table 1**  
Statistical comparison of the PCCs of IMFs.

IMF	Mean PCC	Standard Deviation	Standard Deviation
IMF1 (1.41 kHz to 44.8 kHz)	0.99	0.016	± 1.6 %
IMF2 (1.19 kHz to 14.3 kHz)	0.90	0.113	± 12.5 %
IMF3 (150 Hz)	0.764	0.222	± 28.8 %
IMF4 (50 Hz)	0.58	0.273	± 47 %
IMF5 (50 Hz)	0.504	0.299	± 60 %

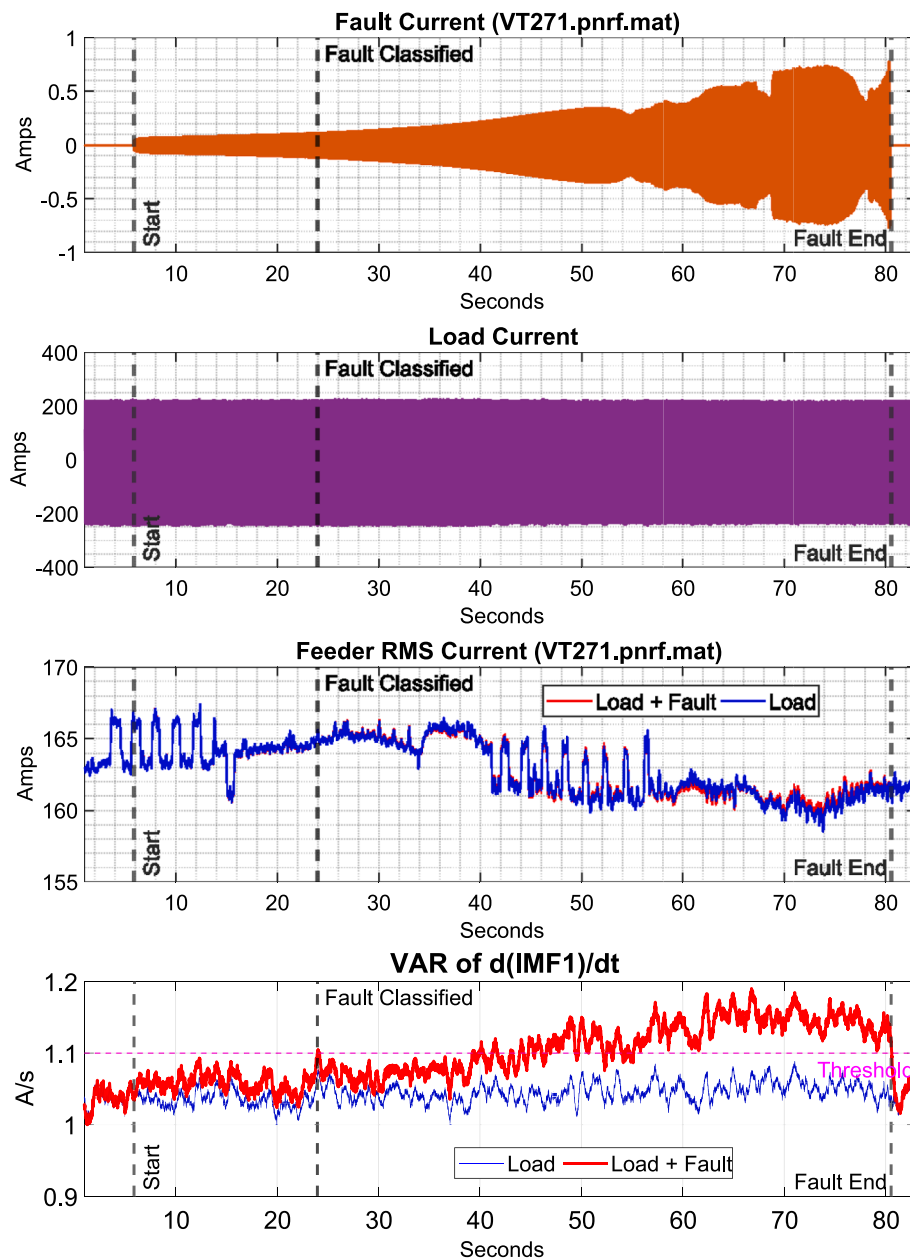


**Fig. 14.** Classification of VT271 (0.5 A limit, Eu. Baxteri). First Row:  $I_f$ . Second Row:  $I_L$ . Third Row: Rolling RMS currents of  $I_L$  and  $(I_L + I_f)$ . Fourth Row: Volatility of the (i)  $I_L$  only (blue trace) case (ii)  $I_L + I_f$  (red trace) case. (For interpretation of the references to colour in this figure legend, the reader is referred to the web version of this article.)

The mean PCC for IMF2 is also high at 0.9 but with an STD of  $\pm 12.5\%$ . IMF3 has a 28.8 % standard deviation relative to its mean 0.76. The two 50 Hz IMF sub-bands have mean PCCs of 0.58 and 0.5, respectively. However, both IMF4 and IMF5 have very high STDs rendering them unreliable as indicators. In conclusion, IMF1, with its near-perfect mean PCC and low STD, is an ideal and reliable EMD sub-band for VeHIF induced volatility detection.

#### 8. Classifying a VeHIF through volatility analysis

During the project [8], only  $I_f$  was sampled in an unloaded feeder with no recordings of any load data. As such, the load data ( $I_L$ ) used herein was separately sourced from a 22 kV substation at the University using a 50 kHz bandwidth AC flex current probe. The probe was connected to a data logger with a Low-Pass filter of 50 kHz cut-off frequency, and sampled the current at 100 kSa/s.

The verification methodology relied on superimposition of the  $I_f$  and  $I_L$  datasets in measuring the volatility-variance of the IMF1 sub-band using (3) and (4). Fig. 13 shows the sampled  $I_f$ ,  $I_L$  and their 100 ms rolling RMS over a 83 s period. Fig. 13 also displays the rolling variance average of IMF1's rate of change. VT963 is a 2 A<sub>rms</sub> limit fault of the C. Glaucomphalus species. Fault inception occurred at 4.53 s into the recording. At the time of classification,  $I_{f,\text{rms}}$  was 0.25 A<sub>rms</sub>. One can see in Fig. 13 that the variances of the two channels is common for both the  $I_L$  (no-fault) and  $I_f + I_L$  (fault) cases in the 0 s to 4.53 s period. The variance of  $I_L$ 's volatility is fluctuating around a mean of 1.0419 A/s with an STD of 0.0137 A/s (no-fault case). After inception at 4.53 s, the variance of  $(I_f + I_L)$ 's volatility deviates from that of the no-fault case and starts to increase. This increase is largely due to the volatility of the fault induced HF components in the IMF1 sub-band. IMF1's volatility variance has an STD of 0.0299 A/s over a mean of 1.1216 A/s. A threshold of 1.1 A/s was selected for classifying the fault ( $I_f + I_L$ ) case



**Fig. 15.** The branch at 24 s into the recording. The branch is yet to experience any charring, any breakout of flames, and no embers are being shed (VT271).

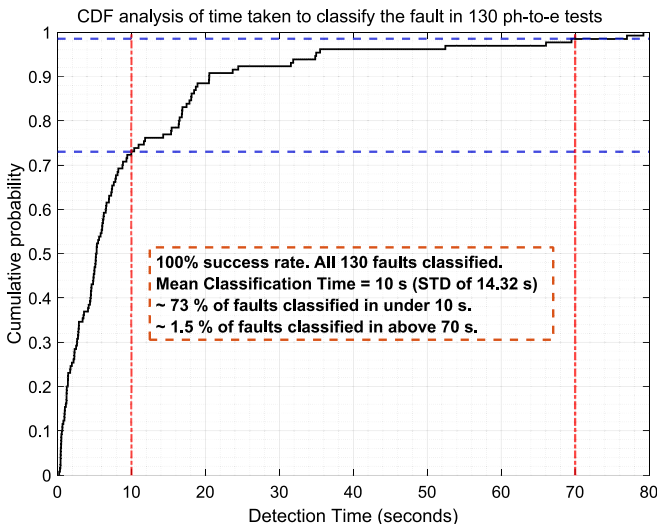


**Fig. 16.** CDF analysis of time to detection metrics of 130 ph-to-e faults.

from the no-fault ( $I_L$ ) case. Fault classification occurred 7.3 s into the recording with a response time of 2.77 s.

**Fig. 14** shows the same volatility-variance analysis for VT271 (0.5 A limit, Eu. Baxteri). For VT271, the classification occurs 24 s into the recording, giving a detection time of 18.1 s. When the fault was classified,  $I_{f,\text{rms}}$  was 78 mA<sub>rms</sub>. The slower, progressive increase of  $I_f$  in VT271 (as compared to VT963) is clearly the cause of this increased response time. The response time in VT271 is 18.1 s, as compared to 2.77 s in VT963. Despite taking 18.1 s to classify the fault (i.e. VT271), **Fig. 14** shows that the fault was still in Stage 1 when classified and had not even reached its first maximum yet. Nevertheless, the proposed protection scheme was effective in classifying the fault, before Stage 3 began.

In Stage 3, a branch generally undergoes carbonisation with a breakout of flames (i.e. increased bushfire risk due to the ember formation). While the method took 18.1 s to classify (i.e. due to low  $I_f$ ), the fault was classified before the fire ignition risk grew. This further satisfies the Marxsen condition [8] for earth fault detection to occur within 2 s of reaching an  $I_f$  of 0.5-A<sub>rms</sub> for tenfold reduction in the fire risk. While taking 18.1 s to classify,  $I_{f,\text{rms}}$  was 78 mA<sub>rms</sub> at the classification time. Therefore, classification occurred, when fire risk was lower, well before  $I_f$  grew to 0.5-A<sub>rms</sub>. **Fig. 15** validates this by providing a visual image of the branch at 24 s into the recording. As shown in **Fig. 15**, there were no flames/embers at 24 s into the recording. In summary, the proposed method may take relatively long to classify some VeHIFs, especially those with slow  $I_f$  growth. Yet, it classifies before localised burning begins on the branch.

$$\sigma_{IMF1}^2(n) = \text{Var} \left( \frac{dI_{IMF1}}{dt}(i + 1 - VRate) : \frac{dI_{IMF1}}{dt}(i) \right) \quad (3)$$

for i = VRate : VRate : length(Current) - VRate

$$vol_{indIMF1}(j) = \frac{1}{N} \times \sum_{k=j}^{j-1+N} \sigma_{IMF1}^2(k) \quad (4)$$

for j ≥ 1, N = 1000, and VRate = 50

The method was applied to a dataset of 130 ph-to-e recordings (a mix of 0.5, 1, and 2 A<sub>rms</sub> limit tests) with a 100 % success rate. **Fig. 16** shows the CDF of response times. All 130 tests were classified with a mean

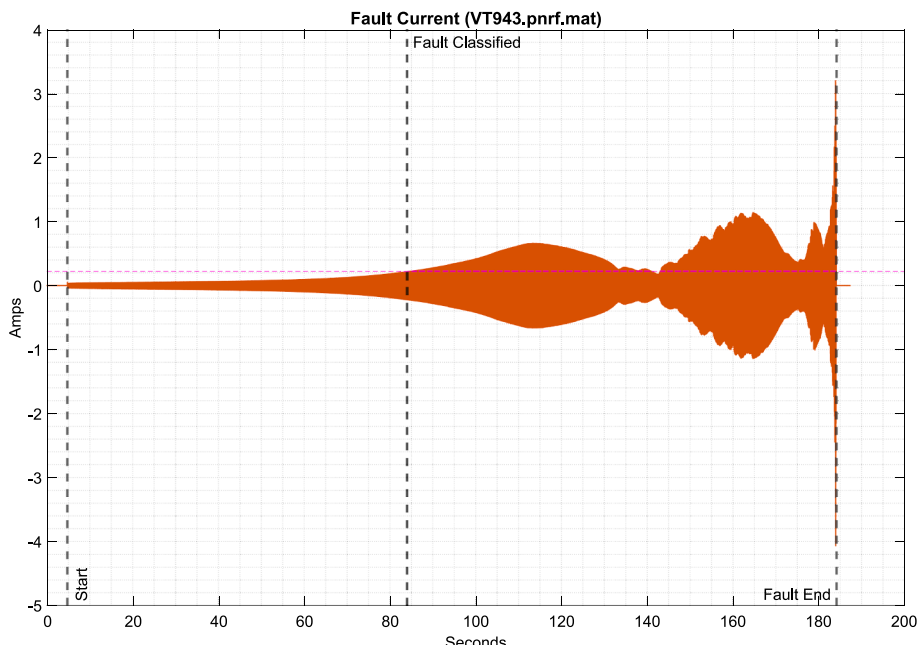


**Fig. 17.** Test with the longest classification duration of 79.24 s (VT943; 2 A<sub>rms</sub> limit test of F. Angustifolia species.



**Fig. 18.** Visual status of the branch of F. Angustifolia at the classification time (image at 84 s into the recording) showing the branch yet to experience any charring. There were no breakout of flames or embers at classification.

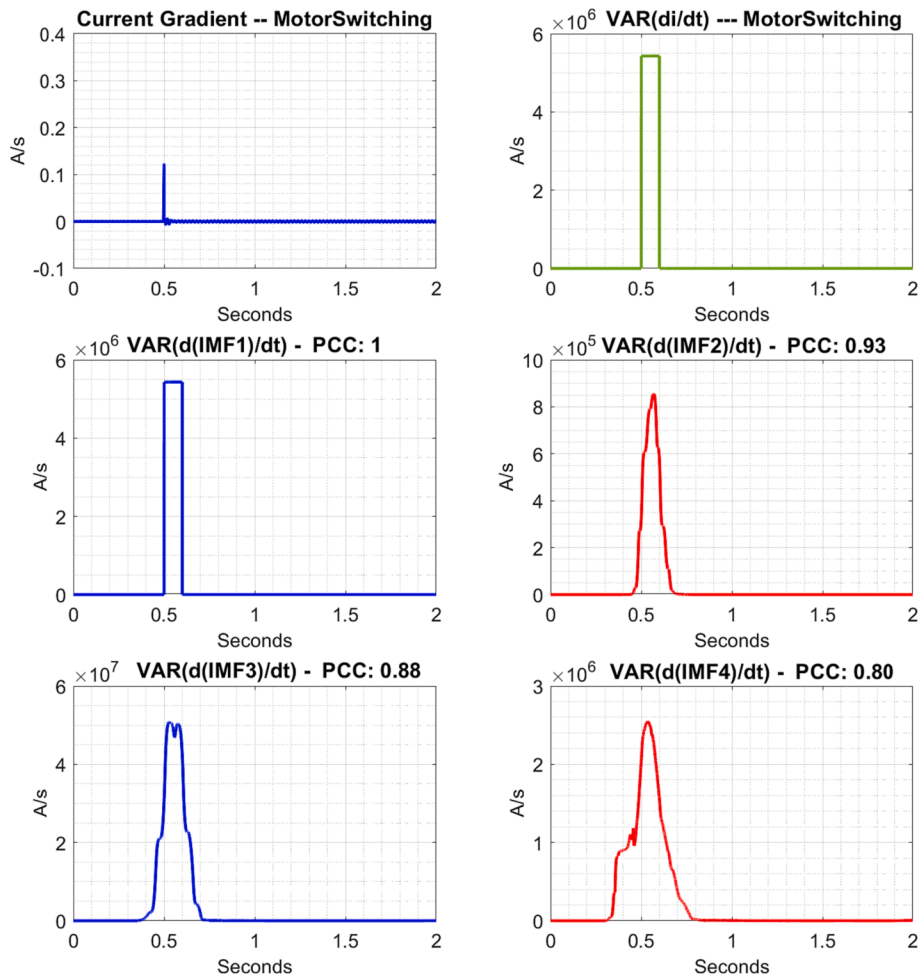


**Fig. 19.** Volatility variance during asynchronous machine switching.

classification time of 10 s (STD of 14.32 s). 73 % of the tests were classified in under 10 s (with reference to the fault start times). Only 1.5 % of the tests were classified in a duration longer than 70 s. Fig. 17 shows the  $I_f$  waveform during VT943 (test with the longest classification duration of 79.24 s). In VT943, the contact with the conductor occurred at 4.76 s into the recording. The fault was classified at 84 s into the

recording. At classification,  $I_f$  was 0.16 A<sub>rms</sub>, far lower than Marxsen 0.5-A<sub>rms</sub> limit [8]. Hence, this worst-case classification still satisfied the Marxsen condition [8] for earth fault detection to occur within 2 s of  $I_f$  reaching 0.5-A<sub>rms</sub>. The fault was classified before  $I_f$  reached 0.5-A<sub>rms</sub>. Fig. 18 shows a snapshot of the video recording of the test VT943 at the classification time. As shown, there were neither any flames nor any

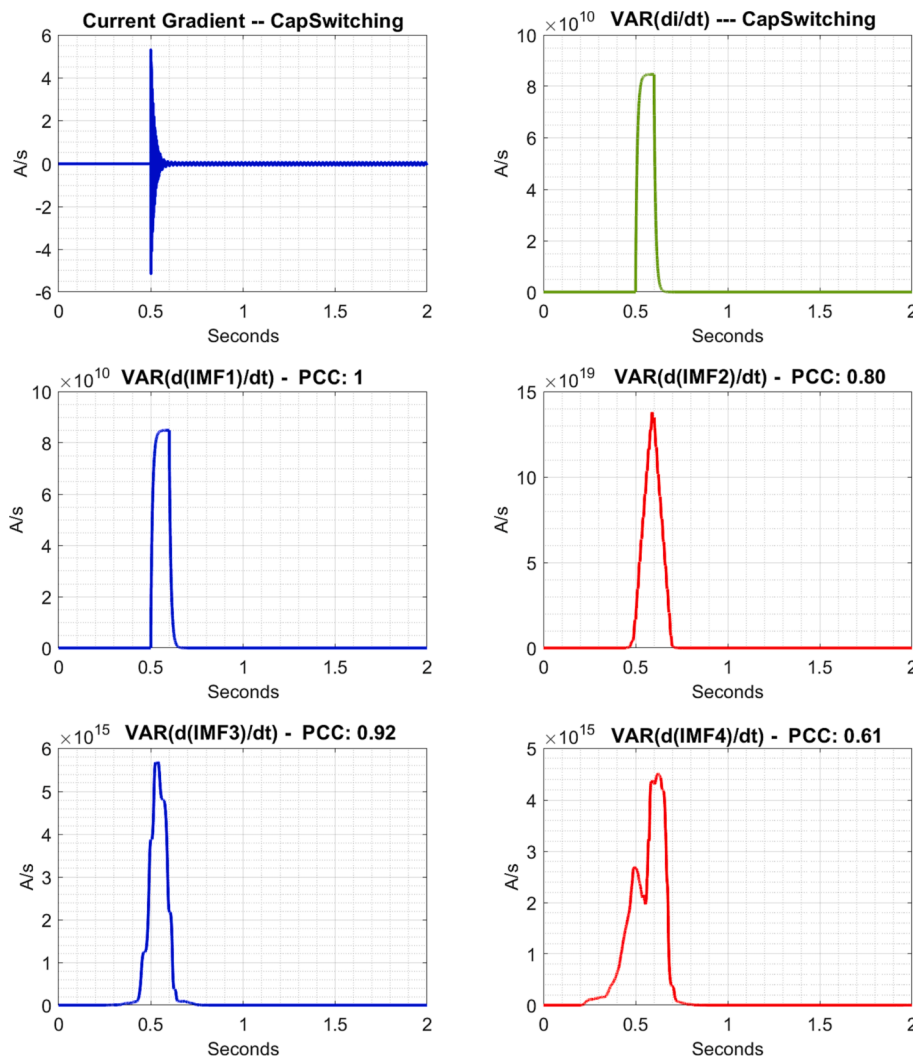


**Fig. 20.** Volatility variance during capacitor bank switching.

embers. Despite taking 79.24 s to classify the fault, the fault was still in Stage 1. The fault was yet to reach Stage 3, when charring and aggressive breakout of flames begins. Therefore, the classification occurred before the fire ignition risk could grow, despite taking longer than a minute.

#### 9. Comparison with other disturbances

HIF indicators could possibly classify other disturbances such as Asynchronous Machine (AS), capacitor bank switching, or starting a Variable Speed Drive (VSD) controlled AC motor. It is critical to distinguish such disturbances from VeHIFs to avoid false positives. This section applies the method to three distinct disturbance cases. A 600 kVar three-phase capacitor bank was modelled in a 5-bus radial 22 kV feeder for simulating the switching transients. For modelling the AS, a 10 HP squirrel-cage induction machine was connected to the 22 kV feeder through a step-down transformer. The third modelled disturbance was a low-voltage VSD controlled AC motor, also connected to the feeder through a step-down transformer. Figs. 19 to 21 show the volatility-variance of all three cases, all switched at 0.5 s. When the switching of the AS machine took place (see Fig. 19), there was a sudden increase in all first four IMFs' rolling volatility-variance. However, all these volatilities either died down or stabilized quickly. It is highly unlikely that sharp spikes will be experienced in all four IMFs during a VeHIF. The short-lived nature of volatility, in other disturbances,

distinguishes them from VeHIFs. As the scheme uses moving averages, short-lived volatility cannot lead to a sustained increase in the volatility index and no subsequent threshold violation can take place. A similar observation can be seen for the capacitor bank switching (see Fig. 20). The variances of first four IMFs' volatility spiked after 0.5 s, but they were not sustained and quickly died down.

For the VSD controlled motor (see Fig. 21), IMF1's volatility-variance stabilisation took longer (around 1.5 s), but also did not match the continuous instability in IMF1's volatility during a VeHIF. This was verified by measuring the rolling variance average of IMF1's volatility using (3) and (4). Fig. 22 shows the sampled  $I_{VSD}$ ,  $I_L$  and their 100 ms rolling RMS over a 10 s period. Fig. 22 also shows IMF1's volatility-variance. As shown, there was no credible change in the volatility-variance indexes of the  $I_L$  (no-disturbance) and  $I_{VSD} + I_L$  (disturbance) cases. The 1.1 threshold level was not violated, resulting in no classification.

#### 10. Discussion of results

In [8], Marxsen argues that earth fault detection within 2 s of  $I_f$  reaching a magnitude of  $0.5 \cdot A_{rms}$  could potentially result in a tenfold reduction in the fire risk. Another conclusion in [8] states that when a species undergoes high degree of charring, the ignition at height is more likely to result in embers with the size and temperature conditions for

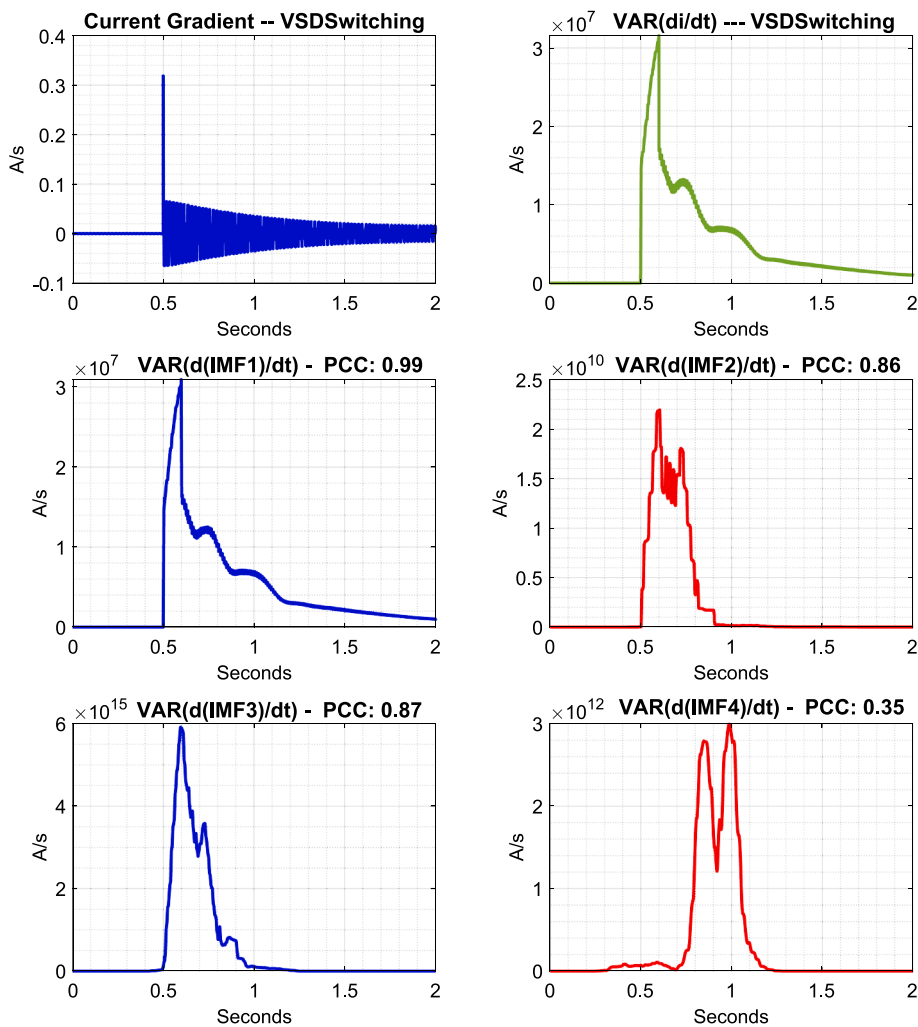


**Fig. 21.** Volatility variance during VSD controlled AC motor switching.

fire ignition at ground level. Herein, author proposed a new method that perfectly satisfied the 2 s criteria, even in slow growth VeHIF cases. The method's effectiveness in detecting VeHIFs (before they progress into localised charring) has been validated through its application to a large dataset of 130 fault recordings. The proposed 'volatility-variance' method relies on rolling variance average of the rate of change in a feeder current's IMF1. The concept examines fluctuations in the volatility of the feeder current's IMF1 data stream. Author applied the proposed method to a dataset of 130 ph-to-e fault recordings with 100 % success and a mean classification time of 10 s (STD of 14.32 s). The proposed scheme classified 23 % of the tests in under 2 s delay and 1.5 % in above 70 s delay. A common distinguishing feature, in VeHIFs taking above the mean detection delay time of 10 s, was the slow  $I_f$  growth. At the classification of these tests,  $I_f$  amplitudes were very low and still in contact development (Stage 1). In the worst-case test example (VT943), fault classification occurred after 79.24 s into the recording. Despite taking so long, the method still classified the fault, before it reached Stage 3 where charring begins. At the time of classification of VT943 as a fault,  $I_f$  was 0.16 A<sub>rms</sub> lower than the 0.5-A<sub>rms</sub> limit discussed above. Hence, the fault was classified prior to the 2 s time limit starting upon  $I_f$  reaching a magnitude of 0.5-A<sub>rms</sub>. Research findings show that classification of VeHIFs by Stage 3 (in the ignition development process) may still result in a significant reduction in the fire risk, irrespective of the length of the detection time.

## 11. Conclusions

This research investigated VeHIFs with conclusions drawn on stages of vegetation ignition development as well as volatility diagnosis for fault detection. The work demonstrates the link between a fault current's volatility and the stages of vegetation ignition development. Volatility and arcing peak as charring of the vegetation branch spreads over the branch. The author then presents EMD of fault currents to validate the near perfect correlation between the volatilities  $I_f$  and the HF components. This validates HF components as the most credible signatures of  $I_f$  volatility during a VeHIF.

A concept, based on the rolling variance average of the rate of change in the first IMF sub-band (IMF1), was later proposed. The method relies on identification of a threshold, from the prior no-fault volatility-variance levels, to discriminate between fault and no-fault conditions. If the threshold level is violated, the scheme signals a fault. The proposed scheme was applied to a dataset of 130 ph-to-e faults with 100 % success and a mean classification time of 10 s (STD of 14.32 s). 23 % of the tests were classified in under 2 s, and 1.5 % classified in above 70 s. While classification should ideally be fast, research findings herein show that classification of VeHIFs by Stage 3 would still result in a significant reduction in the fire risk, irrespective of the length of the detection time. This relates to the various stages of ignition development that a vegetation branch goes through during a VeHIF event. Specifically, it relates to the fact that only in Stage 3, charring begins to spread over a tree branch with a breakout of flames. In the dataset of 130 fault recordings,

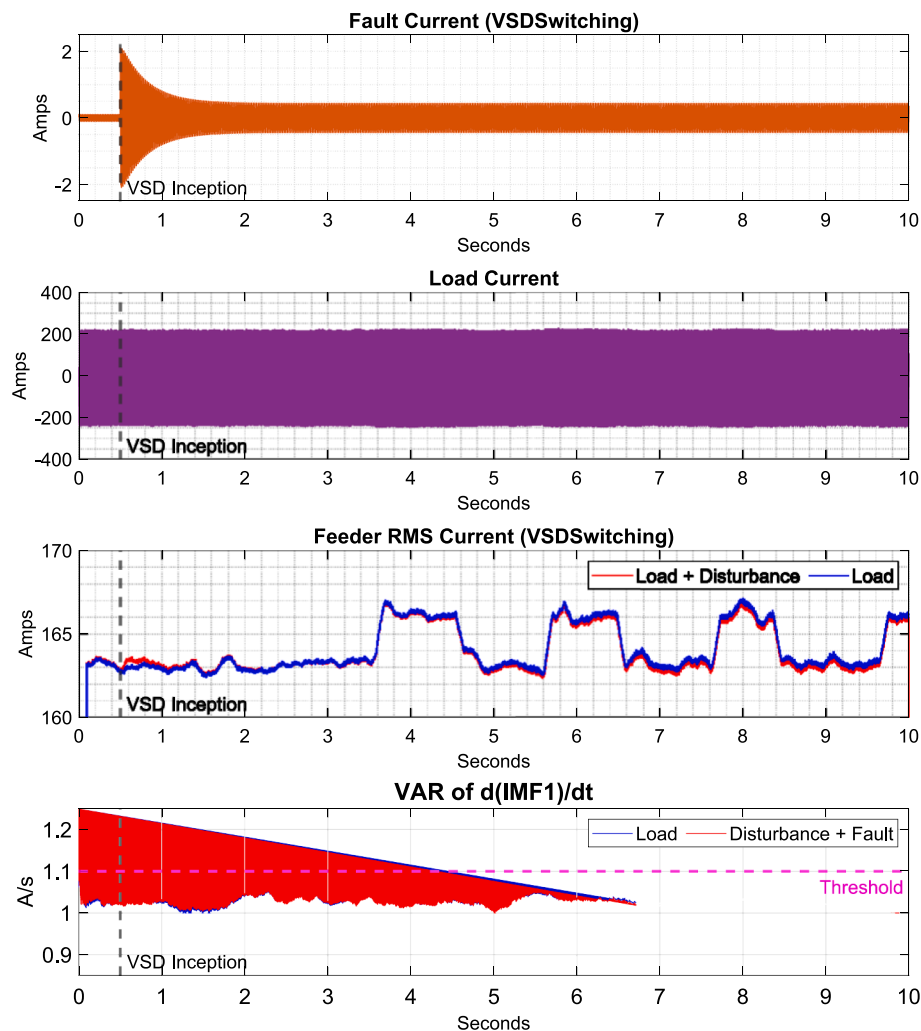


**Fig. 22.** Volatility variance analysis during an event of VSD controlled AC motor switching. First Row: Sampled  $I_{VSD}$ . Second Row: Sampled  $I_L$ . Third Row: Rolling RMS currents of  $I_L$  and  $I_L + I_{VSD}$ . Fourth Row: Volatility analysis of the channel (i)  $I_L$  only case (blue trace) (ii)  $I_L + I_{VSD}$  case (red trace). (For interpretation of the references to colour in this figure legend, the reader is referred to the web version of this article.)

a test labeled as VT943 took the longest (79.24 s into the recording) to classify. When VT943 was classified,  $I_f$  was only 0.16 A<sub>rms</sub> and the fault still was in the contact development stage (Stage 1). The fault was therefore classified before  $I_f$  reached 0.5-A<sub>rms</sub>, a limit after which empirical research shows heightened fire risk.

When a species experiences a high level of charring, this ignition (at height) produces embers that fall to the ground. These falling embers are more likely to fit the size and temperature conditions for fire ignition at the ground level. While the transition time from contact development (Stage 1) to carbonization (Stage 3) varies across different faults, it was the longest in low  $I_f$  growth cases. The low-speed  $I_f$  growth faults were those faults that required long classification times. VeHIF signatures are long lasting, unstable and random. They produce sustained (and growing)  $I_f$  volatility throughout the fault. In other disturbances (e.g. capacitor-bank switching), disturbance signatures are short-lived. They dissipate quickly without being classified, when analysed with the scheme. The proposed method (based on the variance analysis of  $I_f$ 's volatility) is resilient to power-system network disturbances.

#### Declaration of Competing Interest

The authors declare that they have no known competing financial interests or personal relationships that could have appeared to influence the work reported in this paper.

#### References

- [1] C.R. Ozansoy, D.P.S. Gomes, M. Faulkner, Visibility of Vegetation High-Impedance Fault Low-Frequency and High-Frequency Signatures, *IEEE Trans. Power Delivery* 38 (3) (2023) 2236–2239, <https://doi.org/10.1109/TPWRD.2023.3265513>.
- [2] D.P.S. Gomes, C. Ozansoy, High-impedance faults in power distribution systems: A narrative of the field's developments, 2021/12/01/, *ISA Trans.* 118 (2021) 15–34, <https://doi.org/10.1016/j.isatra.2021.02.018>.
- [3] A. Cassie, *Theorie Nouvelle des Arcs de Rupture et de la Rigidité des Circuits, Cigre, Report 102* (1939) 588–608.
- [4] O. Mayr, Beiträge zur Theorie des statischen und des dynamischen Lichtbogens, *Archiv Für Elektrotechnik* 37 (12) (1943) 588–608.
- [5] N.I. Elkalahy, M. Lehtonen, H.A. Darwish, M.A. Izzularab, A.I. Taalab, Modeling and experimental verification of high impedance arcing fault in medium voltage networks, *IEEE Trans. Dielectr. Electr. Insul.* 14 (2) (2007) 375–383, <https://doi.org/10.1109/TDEI.2007.344617>.
- [6] S. Kavaskar, N.K. Mohanty, Detection of High Impedance Fault in Distribution Networks, 2019/03/01/, *Ain Shams Eng. J.* 10 (1) (2019) 5–13, <https://doi.org/10.1016/j.asej.2018.04.006>.
- [7] C. Ozansoy, D.P.S. Gomes, ‘Electrical and physical characterization of earth faults for diverse bush species, 2020/10/01/, *Eng. Sci. Technol. Int. J.* 23 (5) (2020) 1109–1117, <https://doi.org/10.1016/j.jestch.2020.03.002>.
- [8] T. Marxsen, *Vegetation Conduction Ignition Test Report - Final, Marxsen Consulting Pty Ltd, 2015*. Accessed: Nov-2016. [Online]. Available: [https://www.marxsen.com/test-reports/vegetation-conduction-ignition-test-report-final.pdf](#)
- [9] C.R. Ozansoy, D.P.S. Gomes, Volatility Diagnosis in Phase-to-Phase Fault Detection for Branches across Wire Faults, *IEEE Trans. Power Delivery* (2020) 1, <https://doi.org/10.1109/TPWRD.2020.2984217>.
- [10] L. Mingliang, W. Keqi, S. Laijun, Z. Jianju, Applying empirical mode decomposition (EMD) and entropy to diagnose circuit breaker faults, 2015/10/01/, *Optik* 126 (20) (2015) 2338–2342, <https://doi.org/10.1016/j.optik.2015.05.145>.

- [11] A. Patel, P. Shakya, Early fault detection based on empirical mode decomposition method, 2020/01/01/, Procedia CIRP 88 (2020) 31–35, <https://doi.org/10.1016/j.procir.2020.05.006>.
- [12] B. Khorramdel, H. Marzooghi, H. Samet, M. Pourahmadi-Nakhli, M. Raoofat, Fault locating in large distribution systems by empirical mode decomposition and core vector regression, 2014/06/01/, Int. J. Electr. Power Energy Syst. 58 (2014) 215–225, <https://doi.org/10.1016/j.ijepes.2014.01.028>.
- [13] X. Wang, et al., High impedance fault detection method based on improved complete ensemble empirical mode decomposition for DC distribution network, 2019/05/01/, Int. J. Electr. Power Energy Syst. 107 (2019) 538–556, <https://doi.org/10.1016/j.ijepes.2018.12.021>.
- [14] D.A. Gadanayak, R.K. Mallick, Interharmonics based high impedance fault detection in distribution systems using maximum overlap wavelet packet transform and a modified empirical mode decomposition, 2019/11/01/, Int. J. Electr. Power Energy Syst. 112 (2019) 282–293, <https://doi.org/10.1016/j.ijepes.2019.04.050>.
- [15] D.A. Gadanayak, R.K. Mallick, Microgrid differential protection scheme using downampling empirical mode decomposition and Teager energy operator, 2019/08/01/, Electr. Pow. Syst. Res. 173 (2019) 173–182, <https://doi.org/10.1016/j.epsr.2019.04.022>.
- [16] S. Biswal, M. Biswal, O.P. Malik, Hilbert Huang Transform Based Online Differential Relay Algorithm for a Shunt-Compensated Transmission Line, IEEE Trans. Power Delivery 33 (6) (2018) 2803–2811, <https://doi.org/10.1109/TPWRD.2018.2827843>.
- [17] H. Lala, S. Karmakar, Detection and experimental validation of high impedance arc fault in distribution system using empirical mode decomposition, IEEE Syst. J. 14 (3) (2020) 3494–3505, <https://doi.org/10.1109/JSYST.2020.2969966>.
- [18] M. Mishra, P.K. Rout, Detection and classification of micro-grid faults based on HHT and machine learning techniques, IET Gener. Transm. Distrib. 12 (2) (2018) 388–397, <https://doi.org/10.1049/iet-gtd.2017.0502>.
- [19] H. C. Shu, B. Li, Research on Fault Line Detecting Based on Empirical Mode Decomposition (EMD) in Resonant Grounded Systems, in: 2009 Asia-Pacific Power and Energy Engineering Conference, 27–31 March 2009 2009, pp. 1–5, 10.1109/APPEEC.2009.4918686.
- [20] Z. Wang, J. Guo, Y. Zhang, R. Luo, Fault diagnosis for jointless track circuit based on intrinsic mode function energy moment and optimized LS-SVM, in: 2016 IEEE International Conference on High Voltage Engineering and Application (ICHVE), 19–22 Sept. 2016 2016, pp. 1–4, 10.1109/ICHVE.2016.7800578.
- [21] J. A. Wischkaemper, C. L. Benner, and B. D. Russell, “Electrical characterization of vegetation contacts with distribution conductors - investigation of progressive fault behavior,” in 2008 IEEE/PES Transmission and Distribution Conference and Exposition, 21–24 April 2008 2008, pp. 1–8, 10.1109/TDC.2008.4517149.
- [22] O. B. Fosso and M. Molinas, “EMD Mode Mixing Separation of Signals with Close Spectral Proximity in Smart Grids,” in 2018 IEEE PES Innovative Smart Grid Technologies Conference Europe (ISGT-Europe), 21–25 Oct. 2018 2018, pp. 1–6, 10.1109/ISGTEurope.2018.8571816.
- [23] GE Digital Energy. “F60 Feeder Protection System: Instruction Manual.” [https://na.eventscloud.com/file\\_uploads/051c6b2d1eaff0b7ce9e9d780fcbb198a\\_GEF60.pdf](https://na.eventscloud.com/file_uploads/051c6b2d1eaff0b7ce9e9d780fcbb198a_GEF60.pdf) (accessed 5 April, 2023).
- [24] D. Hou, “Detection of high-impedance faults in power distribution systems,” in 2007 Power Systems Conference: Advanced Metering, Protection, Control, Communication, and Distributed Resources, 2007: IEEE, pp. 85–95.